Available online at www.sciencedirect.com
SCIENCE DIRECT
International Journal of Heat and Mass Transfer 49 (2006) 1073–1082
International Journal of HEAT and MASS TRANSFER
www.elsevier.com/locate/ijhmt

Modeling of non-equilibrium argon–oxygen induction plasmas under atmospheric pressure

Nobuhiko Atsuchi [a], Masaya Shigeta [b], Takayuki Watanabe [b,*]

[a] Department of Nuclear Engineering, Tokyo Institute of Technology, 2-12-1 Ookayama, Meguro-ku, Tokyo 152-8550, Japan
[b] Department of Environmental Chemistry and Engineering, Tokyo Institute of Technology, 4259-G1-22 Nagatsuta, Midori-ku, Yokohama 226-8502, Japan

Received 6 May 2005
Available online 7 November 2005

Abstract

Modeling of induction thermal plasmas has been performed to investigate chemically non-equilibrium effect for dissociation and ionization. Computations were carried out for argon–oxygen plasmas under atmospheric pressure. The thermofluid and concentration fields were obtained by solving two-dimensional modeling. This formulation was presented using higher-order approximation of the Chapman–Enskog method for the estimation of transport properties. A deviation from the equilibrium model indicates that argon–oxygen induction plasmas should be treated as non-equilibrium for dissociation and ionization. The present modeling would give the guidance for the rational design of new material processing using thermal plasmas.

Keywords: Induction thermal plasma; Numerical modeling; Argon–oxygen; Non-equilibrium

1. Introduction

The induction thermal plasma approach has been applied for many fields. Especially attractive recent applications are treatment of harmful waste materials and recovery of useful material from waste [1,2]. Another important application is production of high-quality and high-performance materials, such as synthesis of nanoparticles, deposition of thin films, and plasma spraying [3,4]. Induction thermal plasmas offer unique advantages including high enthalpy to enhance reaction kinetics, high chemical reactivity, oxidation and reduction atmospheres in accordance with required chemical reactions, and rapid quenching (10^6 K/s). These advantages increase the advances and demands in plasma chemistry and plasma processing. However, thermal plasmas have been simply used as high-temperature source, because argon is typically used as the plasma gas. In some applications such as reactive plasma spraying, material synthesis, and waste treatment, thermal plasmas with adding reactive gas are desirable to enhance the chemical reactivity of the plasma.

Thermal plasmas have been mainly treated as equilibrium conditions even though sophisticated modeling considering chemical reactions has been required for industrial applications. Some modeling works of induction thermal plasmas including chemical reaction kinetics have been proposed: reactions between $SiCl_4$ and H_2 [5], dissociation of $SiCl_4$ [6,7], dissociation and recombination of finite-rate of diatomic gas in argon plasmas [2,8–12], ionization and recombination as well as dissociation of N_2 in argon plasmas [13,14], synthesis of ultra-fine powders through the decomposition of $SiCl_4$ [15], ionization of seeded alkali metals [16]. In these works, estimation of thermodynamic and transport properties was oversimplified, therefore, more sophisticated models are required. The oversimplified estimation, such as use of equilibrium properties and use of the first-order approximation of Chapman–Enskog method, would cause errors in the numerical results. In order to improve the accuracy of

* Corresponding author. Tel./fax: +81 45 924 5414.
E-mail address: watanabe@chemenv.titech.ac.jp (T. Watanabe).

0017-9310/$ - see front matter © 2005 Elsevier Ltd. All rights reserved.
doi:10.1016/j.ijheatmasstransfer.2005.07.052

Nomenclature

$\mathbf{B}$	magnetic flux density [T]
C_p	specific heat at constant pressure [J kg^{-1} K^{-1}]
D_i^m	effective diffusion coefficient [m^2 s^{-1}]
D_{ij}	diffusion coefficient between species i and j [m^2 s^{-1}]
$\mathbf{E}$	electric field [V m^{-1}]
h	enthalpy [J kg^{-1}]
$\mathbf{J}$	current density [A m^{-2}]
k_f	reaction rate constant for forward reaction [cm^3 mol^{-1} s^{-1}]
M_i	mass of species i [kg]
p	pressure [Pa]
q_r	radiative intensity [W m^{-3}]
R_r	production rate [kg m^{-3} s^{-1}]
T	temperature [K]
$\mathbf{u}$	velocity [m s^{-1}]
x_i	mole fraction of species i [–]
Y_i	mass fraction of species i [–]
δ	degree of chemical non-equilibrium [–]
η	viscosity [Pa s]
η_h	viscosity of heavy particle [Pa s]
η_e	viscosity of electron [Pa s]
λ	thermal conductivity [W m^{-1} K^{-1}]
λ_{tr}	translational thermal conductivity [W m^{-1} K^{-1}]
λ_{tr}^h	translational thermal conductivity due to heavy particle [W m^{-1} K^{-1}]
λ_{tr}^e	translational thermal conductivity due to electron [W m^{-1} K^{-1}]
λ_{int}	internal thermal conductivity [W m^{-1} K^{-1}]
λ_r	reaction thermal conductivity [W m^{-1} K^{-1}]
ξ	permeability of vacuum [T^2 J^{-1} m^3]
ρ	density [kg m^{-3}]
σ	electrical conductivity [A V^{-1} m^{-1}]
τ	stress tensor [Pa]
$\overline{\mathbf{\Omega}}_{ij}^{(i,j)}$	collision integral between species i and j [m^2]

Subscripts

Ar	argon
O_2	oxygen
O	oxygen atom
i, j	chemical species

thermodynamic and transport properties, higher-order approximation of Chapman–Enskog method was applied for estimation of the transport properties of oxygen plasmas [17]. They presented that the thermal conductivity and the electrical conductivity by higher-order approximation differ from those of the first-order approximation especially over 10 000 K.

In this study, a non-equilibrium modeling of argon–oxygen induction thermal plasmas was developed without chemical equilibrium assumptions. This formulation including the finite-rates of dissociation and ionization is presented using higher-order approximation of Chapman–Enskog method for estimation of the transport properties. The non-equilibrium effects on argon–oxygen plasma characteristics will be discussed with comparison between the chemical non-equilibrium (CNE) and chemical equilibrium (CE) modelings.

2. Numerical formulation

2.1. Thermodynamic and transport properties

The transport properties of argon–oxygen plasmas were obtained from Chapman–Enskog method. Up to now, modelings of induction thermal plasmas have been performed with the first-order approximation of the Chapman–Enskog method because higher-order approximation of Sonine polynomial expansion requires many kinds of collision integrals resulting in the complex formula [18]. The first-order approximation may cause errors especially for electrical conductivity and thermal conductivity of electron translational contribution at high temperature. Therefore, higher-order approximation is used according to the required accuracy. The collision integrals $\overline{\mathbf{\Omega}}_{ij}^{(i,j)}$ were taken from Refs. [19–25] which provide the intermolecular potentials and the fitting data. In the CNE model, the thermodynamic and transport properties are strongly related to the temperature and the composition of the plasma. Therefore, the thermodynamic and transport properties should be estimated considering the diffusion of the species in the plasma at each calculation step until the convergence. In contrast to the complex formulation in the CNE model, the thermodynamic and transport properties in the CE model can be estimated by simple function of only temperature.

The effective diffusion coefficient D_i^m for species i was estimated with Eq. (1) with the first-order approximation of Chapman–Enskog method [18]

$$D_i^m = (1 - Y_i) \Bigg/ \sum_{j \neq i, j=1}^{v} \frac{x_i}{D_{ij}} \tag{1}$$

where x_i and Y_i are the mole fraction and mass fraction of species i, respectively, and D_{ij} is the diffusion coefficient between species i and j. The binary diffusion coefficient was calculated by Eq. (2) [26]

$$D_{ij} = 2.628 \times 10^{-2} \sqrt{\frac{M_i + M_j}{2 M_i M_j}} \frac{T^{1.5}}{\overline{\mathbf{\Omega}}_{ij}^{(1,1)}} \tag{2}$$

where M_i is the mass of species i. The ambipolar diffusion coefficient can be estimated to be the double of the diffusion coefficient of ions, because the electron temperature

is considered equal to the heavy particle temperature in thermal plasmas under atmospheric pressure.

The total thermal conductivity λ consists of the reactive conductivity λ_r and "chemically frozen" conductivity (translational λ_{tr} and internal λ_{int})

$$\lambda = \lambda_{tr} + \lambda_{int} + \lambda_r \tag{3}$$

The reactive and internal conductivities were estimated with the first-order approximation of Chapman–Enskog method [18,27]. The translational thermal conductivity contains the contribution of heavy particles λ^h_{tr} and electron λ^e_{tr}. In this study, λ^h_{tr} was estimated with the second-order approximation of the Chapman–Enskog method [28] and λ^e_{tr} with the third-order approximation as the suggestion by Devote [29]

$$\lambda_{tr} = \lambda^h_{tr} + \lambda^e_{tr} \tag{4}$$

Concentration dependence of the thermal conductivity with oxygen injection was shown in Fig. 1. The thermal conductivity has high values where dissociation and ionization occur.

The viscosity due to electron can be neglected because of the small mass. Consequently, the viscosity can be approximated in the following manner:

$$\eta = \eta_h + \eta_e \cong \eta_h \tag{5}$$

The viscosity was estimated with the first-order approximation of Chapman–Enskog method [18]. Concentration dependence of the viscosity with oxygen addition was shown in Fig. 2. The viscosity increases with temperature up to the temperature where ionization plays an important role.

The electrical conductivity requires the third-order approximation for the estimation [29]. The electrical conductivity increases above the temperature where the ionization takes place. The radiative intensity of argon and oxygen was taken from Refs. [30,31].

The thermodynamic properties, the enthalpy and the specific heat at constant pressure, were obtained from the

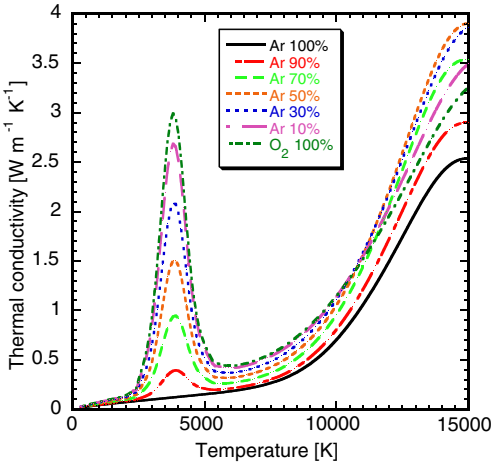

Fig. 1. Thermal conductivity of mixtures of argon and oxygen.

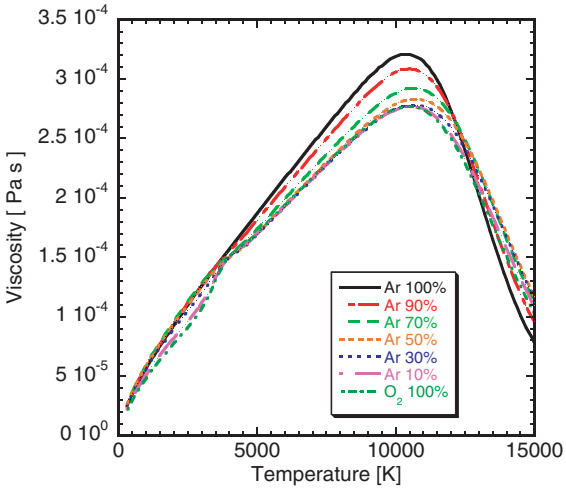

Fig. 2. Viscosity of mixtures of argon and oxygen.

equilibrium properties. This would be oversimplification, however, the accurate estimation of the non-equilibrium thermodynamic properties is very complex with satisfying the self-consistent conditions since concentration of species need to be differentiated by temperature.

2.2. Kinetic rate constants

The considered dissociation of oxygen is the following four kinds of three-body reactions. From the estimation of the equilibrium composition using FACT (Center for Research in Computational Thermochemistry), six species of Ar, Ar^+, O, O_2, O^+, and e^- were considered in this study

$$O_2 + O_2 \rightarrow O + O + O_2 \tag{6}$$

$$O_2 + O \rightarrow O + O + O \tag{7}$$

$$O_2 + Ar \rightarrow Ar + O + O \tag{8}$$

$$O_2 + e^- \rightarrow O + O + e^- \tag{9}$$

The ionization of oxygen and argon atoms was assumed to be the main ionization process in this study

$$O + e^- \rightarrow O^+ + e^- + e^- \tag{10}$$

$$Ar + e^- \rightarrow Ar^+ + e^- + e^- \tag{11}$$

Under the operating condition of the present study, production of ozone is considered to be neglected since the concentration of ozone is negligible enough compared with the concentrations of the other species. The presence of ozone does not affect the transport properties of plasmas.

The dissociation and ionization rate of (6)–(10) can be calculated with Eq. (12). The constants in Eq. (12) are presented in Table 1 taken from Refs. [32,33].

$$k_f = a_l T^{b_l} \exp(-c_l/T) \tag{12}$$

The ionization rate of reaction (11) can be calculated by Eq. (13), which is taken from Ref. [34]

Table 1
Chemical reactions in an argon–oxygen plasma

No.	Reaction	a_l	b_l	c_l
1	$O_2 + O_2 \rightarrow O + O + O_2$	2.0×10^{21}	−1.5	59 500
2	$O_2 + O \rightarrow O + O + O$	1.0×10^{22}	−1.5	59 500
3	$O_2 + Ar \rightarrow Ar + O + O$	1.0×10^{22}	−1.5	59 500
4	$O_2 + e^- \rightarrow O + O + e^-$	9.68×10^{22}	−2.0	59 500
5	$O + e^- \rightarrow O^+ + e^- + e^-$	3.91×10^{33}	−3.78	158 500
6	$Ar + e^- \rightarrow Ar^+ + e^- + e^-$	k_f is taken from Ref. [34]		

$$k_f = 1.68 \times 10^{-20} T^{1.5} \left(\frac{135\,300}{T} + 2 \right) \exp\left(-\frac{135\,300}{T} \right) \tag{13}$$

The recombination rate constants were calculated using the equilibrium constant.

2.3. Model and assumptions

The geometry of the calculation domain of the induction plasma torch was shown in Fig. 3 and the operating conditions are summarized in Table 2. The plasma torch consists of a water-cooled quartz tube and a water-cooled induction coil. The coil consists of three turns and applies the induction frequency at 4 MHz to the plasma. The actual power level was assumed to be 5 kW. Argon–oxygen mixture (oxygen 10% or 30%) is injected as the plasma supporting gas (13 NL/min) and as the sheath gas (20 NL/min). The sheath gas injected with swirl from outer slots protects the inner surface of the quartz tube.

The calculations are based on the following assumptions to derive the governing equations: (a) steady-state laminar flow; (b) axial symmetry; (c) optically thin; (d) negligible viscous dissipation in energy equation; (e) negligible displacement current in comparison with the conductive current; (f) negligible flow-induced electric field; (g) same temperature of heavy particles and electrons.

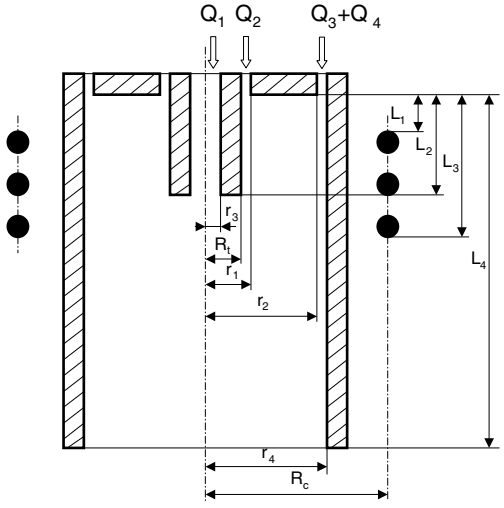

Fig. 3. Geometry of calculation domain of induction plasma torch.

Table 2
Torch characteristic dimensions and operational condition

Torch power	5 kW
Work frequency	4 MHz
Reactor pressure	101.3 kPa
Coil radius	32 mm
Coil turn number	3
Wall thickness of quartz tube	1.5 mm
Distance to frontal end of coil (L_1)	19 mm
Distance to rear end of coil (L_3)	65 mm
Insertion length of probe (L_2)	45 mm
Torch length (L_4)	190 mm
Outer radius of inner slot (r_1)	6.5 mm
Outer radius of outer slot (r_2)	21 mm
Inner radius of injection tube (r_3)	1 mm
Inner radius of quartz tube (r_4)	22.5 mm
Outer radius of injection tube (R_i)	4.5 mm
Flow rate of carrier gas (Q_1)	0 l/min
Flow rate of plasma gas (Q_2)	3 l/min
Flow rate of plasma gas (Q_3)	10 l/min
Flow rate of sheath gas (Q_4)	20 l/min

These assumptions were adopted only for the simplicity. Detailed discussion of two-temperature effect was investigated by Mostaghimi et al. [35]. They found that the deviations from local thermodynamic equilibrium (LTE) for ionization at 30 kPa were large, however the bulk of induction plasmas at atmospheric pressure were close to LTE conditions for ionization. Therefore, the induction plasmas of this study can be treated with a single temperature model, because the pressure is atmospheric pressure. Effect of turbulence was reported by Chen and Boulos [36] as well. They reported that most of the flow field in induction plasmas is laminar at the Reynolds number is 625 at the gas inlet, while the turbulence effect is large at the Reynolds number is 3125. The flow field of the present induction plasmas can be considered as laminar, because the inlet Reynolds number is 350 in this study.

2.4. Governing equations and boundary conditions

The fields of flow, temperature, and concentration in the induction thermal plasma were calculated by solving the two-dimensional continuity, momentum, energy, and species conservation equations coupled with the Maxwell's equations. Chemical reactions of the dissociation and recombination as well as the ionization were taken into account in this modeling.

Continuity:

$$\nabla \cdot (\rho \mathbf{u}) = 0 \tag{14}$$

where ρ is the density and $\mathbf{u}$ is the velocity.

Momentum:

$$\rho \mathbf{u} \cdot \nabla \mathbf{u} = -\nabla p + \nabla \tau + \mathbf{J} \times \mathbf{B} \tag{15}$$

where p is the pressure and $\boldsymbol{\tau}$ is the viscous stress tensor. The last term in the right-hand side expresses the Lorentz force.

Energy:

$$\rho \mathbf{u} \cdot \nabla h = \nabla \cdot \left(\frac{\lambda}{C_p} \nabla h \right) + \mathbf{J} \cdot \mathbf{E} - q_r \tag{16}$$

where h is the enthalpy, λ is the thermal conductivity, C_p is the specific heat at constant pressure, and q_r is the radiation loss per unit volume.

Species:

$$\rho \mathbf{u} \cdot \nabla Y_i = \nabla \cdot (\rho D_i^m \nabla Y_i) + R_{ri} \tag{17}$$

where R_r is the source term owing to the dissociation, recombination and ionization. In these equations, the conduction current $\mathbf{J}$, the magnetic flux density $\mathbf{B}$, and the electric field intensity $\mathbf{E}$ were obtained from Maxwell's equation.

The electromagnetic (EM) field in this study was analyzed on the basis of the two-dimensional modeling approach with the electric field intensity as the fundamental EM field variable [37]. Maxwell's equations are expressed in terms of the electric field intensity as follows

$$\nabla^2 \mathbf{E} - \xi \sigma \frac{\partial \mathbf{E}}{\partial t} = 0 \tag{18}$$

where ξ is the magnetic permeability and σ is the electrical conductivity. The associated boundary conditions for the EM fields are identical to Ref. [37].

The boundary conditions along the centerline were set to insure the axial symmetry. At the wall of the plasma torch, no slip conditions are maintained for the velocity, and the concentrations have zero gradient. The temperature at the inside wall of the plasma torch was calculated assuming the outside wall was maintained at 300 K by water cooling. The injection tube was assumed to be at 500 K. The outflow boundary conditions at the torch were assumed that gradient of the variables are zero. The sheath gas has swirl velocity component. Each gas stream has constant axial velocity with zero radial velocity having temperature at 300 K.

2.5. Calculation procedure

The governing conservation equations were solved using SIMPLER (semi-implicit method for pressure linked equation revised) algorithm [38]. The governing equations and the electric field intensity equation with the associated boundary conditions were discretized into a finite difference form using the control-volume technique. Non-uniform grid points 30 by 30 were used for radial and axial directions, respectively. Grids are made finer close to the center and the coil region. Thermodynamic and transport properties were calculated from the temperature and compositions at each position in the calculation domain at each iteration step.

3. Calculation results

Computations were performed for pure argon, argon–oxygen (oxygen 10%), and argon–oxygen (oxygen 30%) plasmas operated under atmospheric pressure by comparing of the CNE and CE models. The calculated temperature fields were presented in Figs. 4–6. The upper side in each figure presents the CNE calculation, and the lower side is derived by the CE calculation. The high-temperature region in the torch is shrunk with oxygen injection. This is attributed to oxygen dissociation around 4000 K, because the higher heat capacity including the dissociation of oxygen leads to the temperature decrease. Dissociation of oxygen also leads to a decrease of heat loss at the wall due to the more moderate temperature gradient of an argon–oxygen plasma near the torch wall than that of an argon plasma, which results in higher energy efficiency of argon–oxygen plasmas. From the comparison between the CNE and the CE calculation, the temperature deviation of CNE model from CE model is not negligible in the argon–oxygen (oxygen 30%) plasma, although the

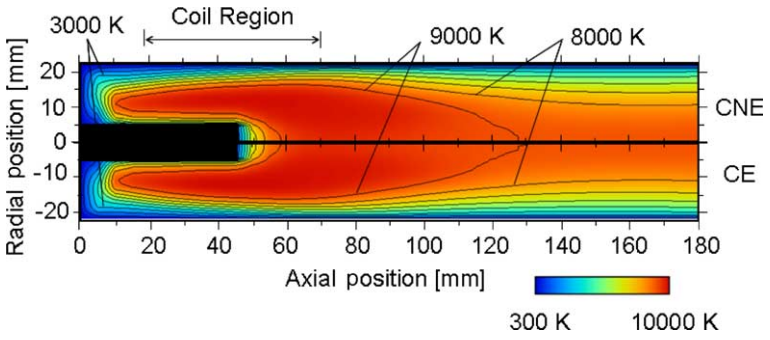

Fig. 4. Comparison of isotherms of chemical equilibrium and chemical non-equilibrium models for an argon plasma at 4 MHz and 5 kW. All isotherms are divided by 1000 K.

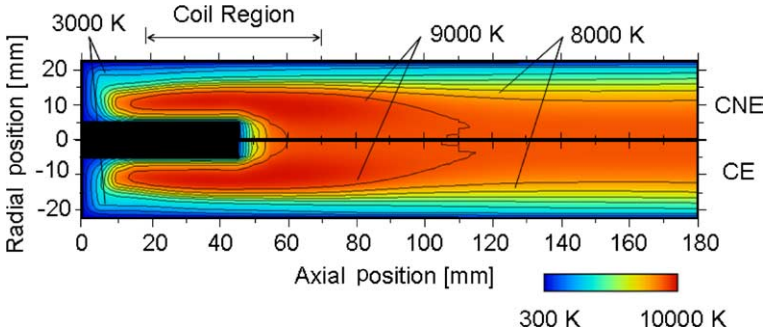

Fig. 5. Comparison of isotherms of chemical equilibrium and chemical non-equilibrium models for an argon–oxygen plasma (oxygen 10%) at 4 MHz and 5 kW. All isotherms are divided by 1000 K.

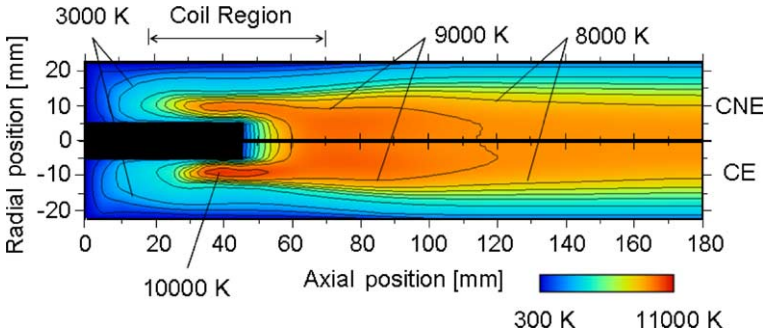

Fig. 6. Comparison of isotherms of chemical equilibrium and chemical non-equilibrium models for an argon–oxygen plasma (oxygen 30%) at 4 MHz and 5 kW. All isotherms are divided by 1000 K.

difference between CNE and CE is small in the pure argon plasma and the argon–oxygen (oxygen 10%) plasma. Compared with the pure argon plasma and the argon–oxygen (10%) plasma, the argon–oxygen (oxygen 30%) plasma has the small high-temperature region over 9000 K at the coil region. This is because the larger energy consumption caused by dissociation of oxygen leads to a larger temperature decrease near the torch wall region. Large effect of particle-diffusion caused by the large concentration gradient leads to the temperature difference between the CNE and the CE models.

The calculated flow field of the argon–oxygen plasma (oxygen 30%) is presented in Fig. 7. The flow fields of the induction plasmas exhibit the characteristic recirculations, because the flows are pinched by the radial Lorentz forces induced at the coil region. The CNE and the CE models display the similar streamlines.

The corresponding concentration profiles of oxygen atoms of the argon–oxygen (oxygen 30%) plasma in Fig. 8 show that the high-concentration region of oxygen atoms coincides almost with the high-temperature region. In the CNE calculation, oxygen atoms also exist the upstream region of the high-temperature region, because of the larger recirculation above the coil region. Besides, the radial concentration gradient of the CNE model is more moderate than that of CE model especially at the coil region. This is due to the diffusion effect, namely, the diffusion rate of dissociated oxygen atoms is much higher than

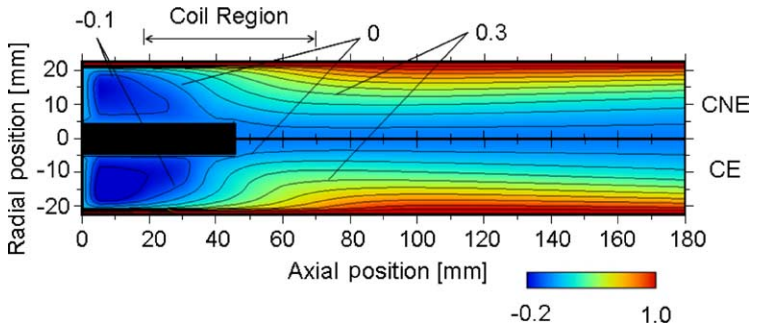

Fig. 7. Comparison of streamlines of chemical equilibrium and chemical non-equilibrium models for an argon–oxygen plasma (oxygen 30%) at 4 MHz and 5 kW. All streamlines are divided by 0.1.

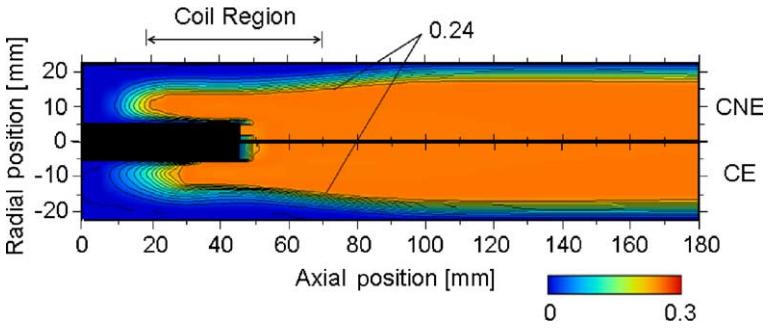

Fig. 8. Comparison of oxygen atom concentration contours of chemical equilibrium and chemical non-equilibrium models for an argon–oxygen plasma (oxygen 30%) at 4 MHz and 5 kW. All contour lines are divided by 0.03.

the chemical reaction rate at the low temperature region such as the torch inlet and near the torch wall region.

The corresponding number density profiles of Ar, Ar^+, O_2, O, and O^+ at the center of the coil are shown in Fig. 9 for oxygen 10% and Fig. 10 for oxygen 30%. The number densities of oxygen atoms and ions near the torch wall show difference between the CE and the CNE models, because the species distribute near coil region due to the radial diffusion in the CNE model. On the other hand, in the plasma high-temperature region, number densities are almost the same between the CNE and the CE calculation. This is because oxygen has low dissociation energy of 5.1 eV. High temperature above 4000 K causes the high chemical reaction rate. In the high-temperature region, the CNE model of the argon–oxygen plasmas can be treated as an equilibrium state.

Effect of chemical reaction kinetics and diffusion on the degree of dissociation of oxygen in the argon–oxygen plasma (oxygen 10%) is presented in Fig. 11. Degree of dissociation shows almost the same profiles between the CNE and the CE models. The degree of ionization of oxygen atoms in the argon–oxygen plasma (oxygen 10%) in the CNE and the CE calculation is shown in Fig. 12. The degree of ionization calculated by the CNE model shows large difference from that by the CE model in the downstream region of the injection tube.

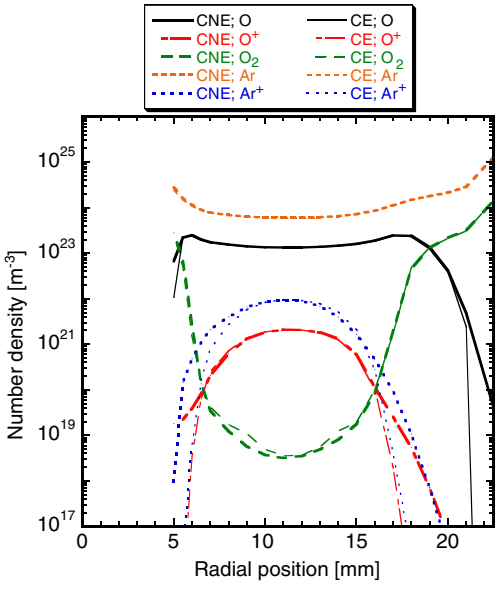

Fig. 9. Effect of chemical reaction kinetics and diffusion on species distribution at the center of the coil in argon–oxygen plasma (oxygen 10%) at 4 MHz and 5 kW.

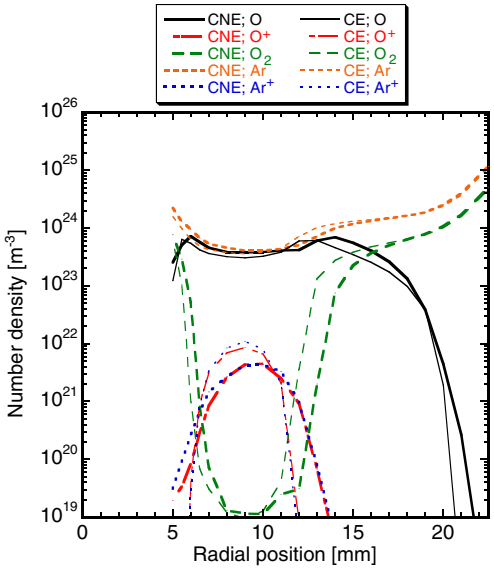

Fig. 10. Effect of chemical reaction kinetics and diffusion on species distribution at the center of the coil in argon–oxygen plasma (oxygen 30%) at 4 MHz and 5 kW.

In this study, the degree of CNE (chemical non-equilibrium) was introduced as follows [39] to demonstrate the deviation between the CNE and the CE models.

Dissociation:

$$\delta^{\mathrm{d}}_{\mathrm{O}_2} = \frac{[\mathrm{O}]^2}{[\mathrm{O}_2]K_{\mathrm{O}}} \tag{19}$$

Ionization:

$$\delta^{\mathrm{i}}_{\mathrm{O}^+} = \frac{[\mathrm{O}^+][\mathrm{e}^-]}{[\mathrm{O}]K_{\mathrm{O_i}}} \tag{20}$$

$$\delta^{\mathrm{i}}_{\mathrm{Ar}^+} = \frac{[\mathrm{Ar}^+][\mathrm{e}^-]}{[\mathrm{Ar}]K_{\mathrm{Ar_i}}} \tag{21}$$

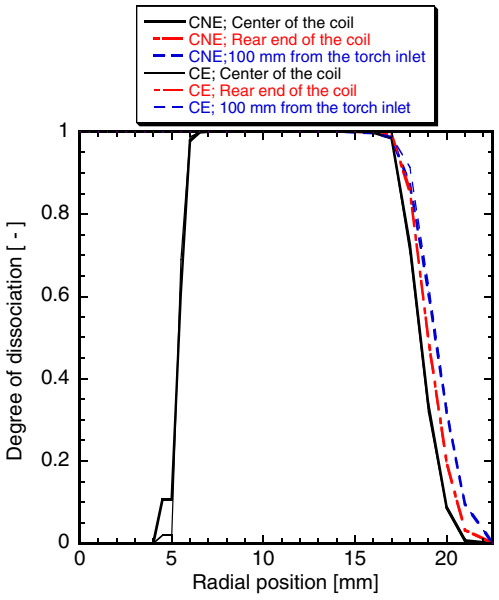

Fig. 11. Effect of chemical reaction kinetics and diffusion on degree of dissociation in argon–oxygen plasma (oxygen 10%) at 4 MHz and 5 kW.

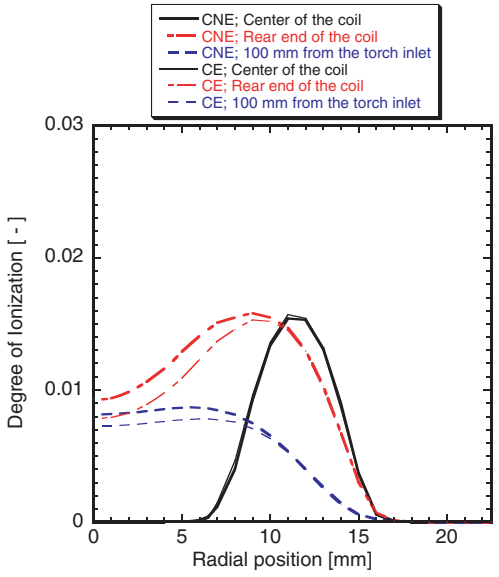

Fig. 12. Effect of chemical reaction kinetics and diffusion on axial degree of ionization in argon–oxygen plasma (oxygen 10%) at 4 MHz and 5 kW.

where [M] is the molar concentration of species M in the plasma, and K is the equilibrium constant. Subscripts O, O_i, and Ar_i respectively represent the oxygen dissociation, oxygen ionization, and argon ionization. Value $\delta = 1$ represents complete equilibrium condition, besides, $\delta > 1$ represents overpopulation of products, and underpopulation of reactants for $\delta < 1$. The calculated degree of CNE due to dissociation is shown in Fig. 13. The degree of CNE deviates from the equilibrium value ($\delta = 1$) in $r > 20$ mm. This indicates that chemical non-equilibrium appears near

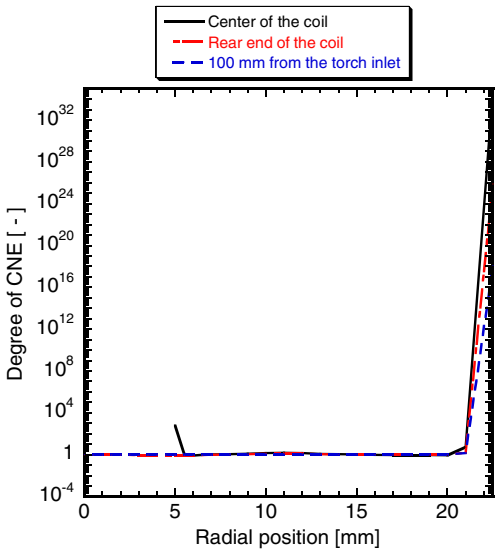

Fig. 13. Degree of CNE due to dissociation in argon–oxygen plasma (oxygen 10%) at 4 MHz and 5 kW.

the torch wall because the diffusion rate is higher than the chemical reaction rate in this region. In contrast with the case of oxygen, a strong non-equilibrium state in argon–nitrogen induction plasmas was reported by Tanaka and Sakuta [13]. They found a large deviation from the CE calculation in the distribution of particle compositions. A strong non-equilibrium state in nitrogen plasmas is reasonable, because nitrogen has relatively higher dissociation energy. However, even for diatomic gas such as oxygen and hydrogen with low dissociation energy, effect of non-equilibrium should be considered for an accurate numerical analysis.

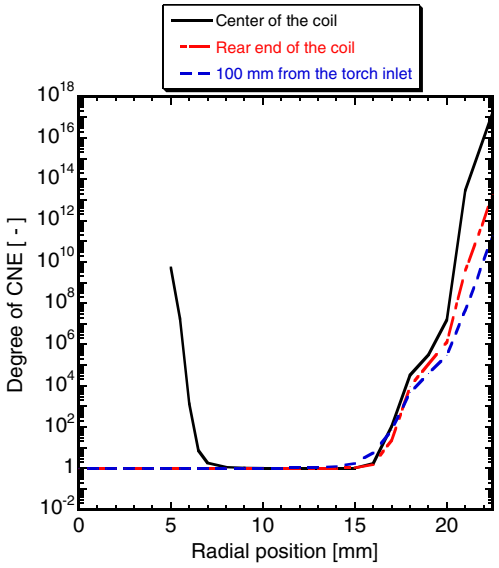

Fig. 14. Degree of CNE due to ionization in argon–oxygen plasma (oxygen 10%) at 4 MHz and 5 kW.

The calculated degree of CNE due to ionization is shown in Fig. 14. The degree of CNE deviates from the equilibrium value ($\delta = 1$) near the torch wall in $r >$ 15 mm as well as dissociation. Ions and electrons scarcely exist, and the degree of ionization is considerably low in this region. Therefore, chemical non-equilibrium caused by ionization is also considerable near the torch wall.

4. Conclusions

A chemically non-equilibrium modeling for argon–oxygen induction thermal plasmas was developed considering effects of diffusion and finite reaction rates without LTE assumption.

The degrees of dissociation with the non-equilibrium model are almost the same with those of the fully equilibrium model at the high-temperature region of argon–oxygen plasmas. This indicates argon–oxygen induction plasmas can be partially treated as equilibrium, but the diffusion effect cannot be negligible near the torch wall. The diffusion effect of the CNE model is as follows; Steep temperature gradient causes moderate concentration gradient. That is why a large number of oxygen atoms exist near the torch wall than the CE model. Furthermore, the degree of CNE was introduced in this study to evaluate the chemical non-equilibrium. From the degree of CNE, a chemical non-equilibrium state appears near the torch wall region due to both dissociation and ionization. Therefore, the present modeling including chemically non-equilibrium would give the guidance for the rational design of new material processing.

References

[1] M. Sakano, M. Tanaka, T. Watanabe, Application of radio-frequency thermal plasmas to treatment of fly ash, Thin Solid Films 386 (2000) 189–194.

[2] M. Sakano, T. Watanabe, M. Tanaka, Numerical and experimental comparison of induction thermal plasma characteristics between 0.5 MHz and 4 MHz, J. Chem. Eng. Jpn. 32 (1999) 619–625.

[3] M. Shigeta, T. Sato, H. Nishiyama, Computational experiment of a particle-laden RF inductively coupled plasma with seeded potassium vapor, Int. J. Heat Mass Transfer 47 (2004) 707–716.

[4] M. Shigeta, T. Watanabe, H. Nishiyama, Numerical investigation for nano-particle synthesis in an RF inductively coupled plasma, Thin Solid Films 457 (2004) 192–200.

[5] G.Y. Zhao, J. Mostaghimi, M.I. Boulos, The induction plasma chemical reactor: Part II. Kinetic model, Plasma Chem. Plasma Process. 10 (1990) 151–166.

[6] J.W. McKelliget, N. El-Kaddah, The effect of coil design on materials synthesis in an inductively coupled plasma torch, J. Appl. Phys. 64 (1988) 2948–2954.

[7] J.W. McKelliget, N. El-Kaddah, Modeling of materials synthesis in hybrid plasma reactors. Production of silicon by thermal decomposition of $SiCl_4$, Metall. Trans. 21B (1990) 589–598.

[8] S.L. Girshick, W. Yu, Radio-frequency induction plasmas at atmospheric pressure: mixtures of hydrogen, nitrogen, and oxygen with argon, Plasma Chem. Plasma Process. 10 (1990) 515–529.

[9] S.L. Girshick, C. Li, W. Yu, H. Han, Fluid boundary layer effects in atmospheric-pressure plasma diamond film deposition, Plasma Chem. Plasma Process. 13 (1993) 169–187.

[10] T. Watanabe, N. Tonoike, T. Honda, A. Kanzawa, Flow, temperature and concentration fields in reactive plasmas in an inductively coupled RF discharge. Characteristics in argon–oxygen and argon–nitrogen thermal plasmas, J. Chem. Eng. Jpn. 24 (1991) 25–32.

[11] T. Watanabe, A. Kanzawa, T. Ishigaki, Y. Moriyoshi, Thermal plasma treatment of titanium carbide powders: Part I. Numerical analysis of powder behavior in argon–hydrogen and argon–nitrogen radio frequency plasmas, J. Mater. Res. 11 (1996) 2598–2610.

[12] M. Desilets, B. Davies, G. Soucy, P. Proulx, Mixing study in an inductive plasma reactor: comparison between model calculations and experimental results, Can. J. Chem. Eng. 76 (1998) 707.

[13] Y. Tanaka, T. Sakuta, Chemically non-equilibrium modeling of N_2 thermal ICP at atmospheric pressure using reaction kinetics, J. Phys. D 35 (2002) 468–476.

[14] Y. Tanaka, Two-temperature chemically non-equilibrium modeling of high-power Ar–N_2 inductively coupled plasmas at atmospheric pressure, J. Phys. D 37 (2004) 1190–1205.

[15] M. Desilets, J.F. Bilodeau, P. Proulx, Modelling of the reactive synthesis of ultra-fine powders in a thermal plasma reactor, J. Phys. D 30 (1997) 1951–1960.

[16] H. Nishiyama, M. Shigeta, Numerical simulation of an RF inductively coupled plasma for functional enhancement by seeding vaporized alkali metal, Eur. Phys. J., Appl. Phys. 18 (2002) 125–133.

[17] T. Watanabe, N. Sugimoto, Numerical analysis of oxygen induction thermal plasmas with chemically non-equilibrium assumption for dissociation and ionization, Thin Solid Films 457 (2004) 201–208.

[18] J.O. Hirschfelder, C.F. Curtiss, R.B. Bird, Molecular Theory of Gases and Liquids, John Wiley, New York, 1964.

[19] E. Mason, Transport properties of gases obeying modified buckingham potential, J. Chem. Phys. 22 (1954) 169–186.

[20] L. Monchick, Collision integrals for the exponential repulsive potential, Phys. Fluids 2 (1959) 695–700.

[21] T. Kihara, M. Taylor, J.O. Hirschfelder, Transport properties for gases assuming inverse power intermolecular potentials, Phys. Fluids 3 (1960) 715–720.

[22] F. Smith, R. Munn, Automatic calculation of the transport collision integrals with tables for the morse potential, J. Chem. Phys. 41 (1964) 3560–3568.

[23] R. Devoto, Transport coefficients of partially ionized argon, Phys. Fluids 10 (1967) 354–364.

[24] H. Milloy, R. Crompton, J. Rees, A. Robertson, The momentum transfer cross section for electrons in argon in the energy range 0–4 eV, Aust. J. Phys. 30 (1977) 61–72.

[25] M. Capitelli, C. Gorse, S. Longo, Collision integrals of high-temperature air species, J. Thermophys. Heat Transfer 14 (2000) 259–268.

[26] R.B. Bird, W.E. Stewart, E.N. Lightfoot, Transport Phenomena, John Willy, New York, 1960.

[27] J.N. Bulter, R.S. Brokaw, Thermal conductivity of gas mixtures in chemical equilibrium, J. Chem. Phys. 26 (1957) 1636–1643.

[28] C. Muckenfuss, C.F. Curtiss, Thermal conductivity of multicomponent gas mixtures, J. Chem. Phys. 29 (1958) 1273–1277.

[29] R.S. Devote, Simplified expressions for the transport properties of ionized monatomic gases, Phys. Fluids 10 (1967) 2105–2112.

[30] R.U. Krey, J.C. Morris, Experimental total and total line radiation of nitrogen, oxygen, and argon plasmas, Phys. Fluids 13 (1970) 1483–1487.

[31] R. Miller, R. Ayen, Temperature profiles and energy balances for an inductively coupled plasma torch, J. Appl. Phys. 40 (1969) 5260–5273.

[32] C. Park, A review of reaction rates in high temperature air, AIAA Paper, 1989, pp. 89–1740.

[33] C. Park, Assessment of two-temperature kinetic model for ionizing air, J. Thermophys. Heat Transfer 3 (1989) 233–244.

[34] M. Hoffert, H. Lien, Quasi-one-dimensional nonequilibrium gas dynamics of partially ionized two-temperature argon, Phys. Fluids 10 (1967) 1769–1777.

[35] J. Mostaghimi, P. Proulx, M.I. Boulos, A two-temperature model of the inductively coupled rf plasma, J. Appl. Phys. 61 (1987) 1753–1760.

[36] K. Chen, M.I. Boulos, Turbulence in induction plasma modeling, J. Phys. D 27 (1994) 946–952.
[37] X. Chen, E. Pfender, Modeling of RF plasma torch with a metallic tube inserted for reactant injection, Plasma Chem. Plasma Process. 11 (1991) 103–128.
[38] S.V. Patanker, Numerical Heat transfer and Fluid Flow, McGraw-Hill, New York, 1980.
[39] C. Chang, J. Ramshaw, Modeling of nonequilibrium effects in a high-velocity nitrogen–hydrogen plasma jet, Plasma Chem. Plasma Process. 16 (1996) 5s–17s.